Inorganic Chemistry

Article

pubs.acs.org/IC

Electron Paramagnetic Resonance Analysis of $La_{1-x}M_xMnO_{3+\delta}$ (M = Ce, Sr) Perovskite-Like Nanostructured Catalysts

Cesare Oliva,* Mattia Allieta, Marco Scavini, Cesare Biffi, Ilenia Rossetti, and Lucio Forni

Dipartimento di Chimica, Università degli Studi di Milano and CNR-ISTM, Via C. Golgi 19, 20133 Milano, Italy

ABSTRACT: The physical-chemical properties of some nanostructured perovskite-like catalysts of general formula $La_{1-x}M_xMnO_{3+\delta}$ (M = Ce, Sr) have been investigated, in particular by using the electron paramagnetic resonance (EPR) technique. We show that the interplay between the -O-Mn^{3+}-O-Mn^{4+}-O- electron double-exchange and the electron mobility is strictly dependent on the dopant nature and the annealing conditions in air. A relationship between the observed properties of these samples and their activity in the methane flameless catalytic combustion is proposed.

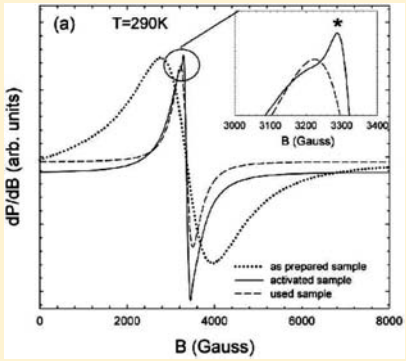

INTRODUCTION

Extensive investigations have been carried out to set up suitable preparation procedures of $La_{1-x}M_xMnO_{3+\delta}$ (M = Ce, Sr) mixed oxides. Indeed, for their practical application as in catalytic flameless combustion (CFC) of hydrocarbons[1] it is compulsory to combine their thermal stability to their high specific surface area (SSA), but the traditional synthesis procedures, like sol–gel (SG), do not allow to impart sufficient thermal resistance to them. In addition, it has been extensively reported that the preparation procedure of these mixed oxides deeply influences also the stabilization of unusual oxidation states for the B metal ion in the $ABO_{3+\delta}$ perovskites (where, in the present case, A = La and B = Mn), as well as the formation of activated oxygen species.[2] Furthermore, a different incorporation degree of the ion A′, possibly substituting for A, can be achieved, depending on the synthesis conditions.[3,4]

Concerning the use of these materials as catalysts for hydrocarbon CFC,[5] we must outline also that a satisfactory catalytic performance may be attained at high temperature only because of oxygen mobility through the perovskite-like lattice.[6] On the other hand, tight relationships exist between lattice structure and magnetic and electronic properties of these crystals,[7,8] as well as between their defect chemistry and transport properties. Nevertheless, univocal interpretation of these relationships has not been proposed yet.

Furthermore, doping with ions of a different oxidation state deeply influences the oxidation state of Mn cations, the defect chemistry of the compound, and, therefore, its catalytic performance. In particular, partial substitution of Sr^{2+} for La^{3+} favors the oxidation of some Mn^{3+} to Mn^{4+}, providing new physical-chemical properties to the sample, among which a higher conversion for the CFC of methane.[5,6] The opposite case is that of M^{4+} ions (like Ce^{4+}) substituting for La^{3+}. In the latter situation some Mn^{3+} may reduce to Mn^{2+}, for charge balancing.[8] In the present investigation, $La_{1-x}M_xMnO_{3+\delta}$ (x = 0, $x \cong 0.1$ with M = Ce; $x \cong 0.1$ and $\cong 0.2$ with M = Sr) samples have been prepared by the Flame Pyrolysis (FP) procedure,[5,9,10] so to obtain nanosized ($d_p \cong 20$ nm) particles of high SSA. The catalysts have been thoroughly investigated by electron paramagnetic resonance spectroscopy (EPR) and X-ray powder diffraction (XRPD and HRPD). A deep analysis of the EPR spectral shape and of its change with temperature and with chemical reaction is also attempted. The aim of the present work was to highlight the relations between some structural and magnetic properties of FP-prepared Ce- and Sr-doped La-manganites and their performances as catalysts for the CFC of methane.

EXPERIMENTAL SECTION

Catalyst Preparation. The $La_{1-x}M_xMnO_{3+\delta}$ samples have been synthesized by FP from proper solutions prepared by dissolving the salts of the metals in propionic acid (Aldrich, pur. 97%). The salts were $La(CH_3COO)_3{\cdot}2H_2O$ (Aldrich, pur. 99.9%), $Mn(CH_3COO)_2{\cdot}4H_2O$ (Aldrich, pur. 99.9%), $Sr(CH_3COO)_2$ (Aldrich, pur. 99%), $Ce(CH_3COO)_3$ (Aldrich, pur. 99.9%).

Catalyst composition has been determined by scanning electron microscopy-energy dispersive X-ray spectroscopy (SEM-EDX) analysis and in particular it resulted in x = 0.1(1) for Sr and 0.1(5) for Ce. Since the M = Sr sample was the most interesting from the catalytic point of view,[5] we decided to determine more accurately its actual composition by inductively coupled plasma mass spectrometry (ICP-MS) (Perkin-Elmer ELAN 6000 instrument) after mineralization with HNO_3 under microwave irradiation. x = 0.100(1) was found for this sample. Besides, we prepared one more sample with a higher amount of Sr, that is, with x = 0.19(1) (by ICP-MS).

The FP apparatus has been described in detail elsewhere.[10] The solution feeding rate was 4.4 mL min^{-1} and the O_2 flow rate was 5 L

Received: May 11, 2012
Published: July 16, 2012

   dx.doi.org/10.1021/ic300977e | *Inorg. Chem.* 2012, 51, 8433–8440

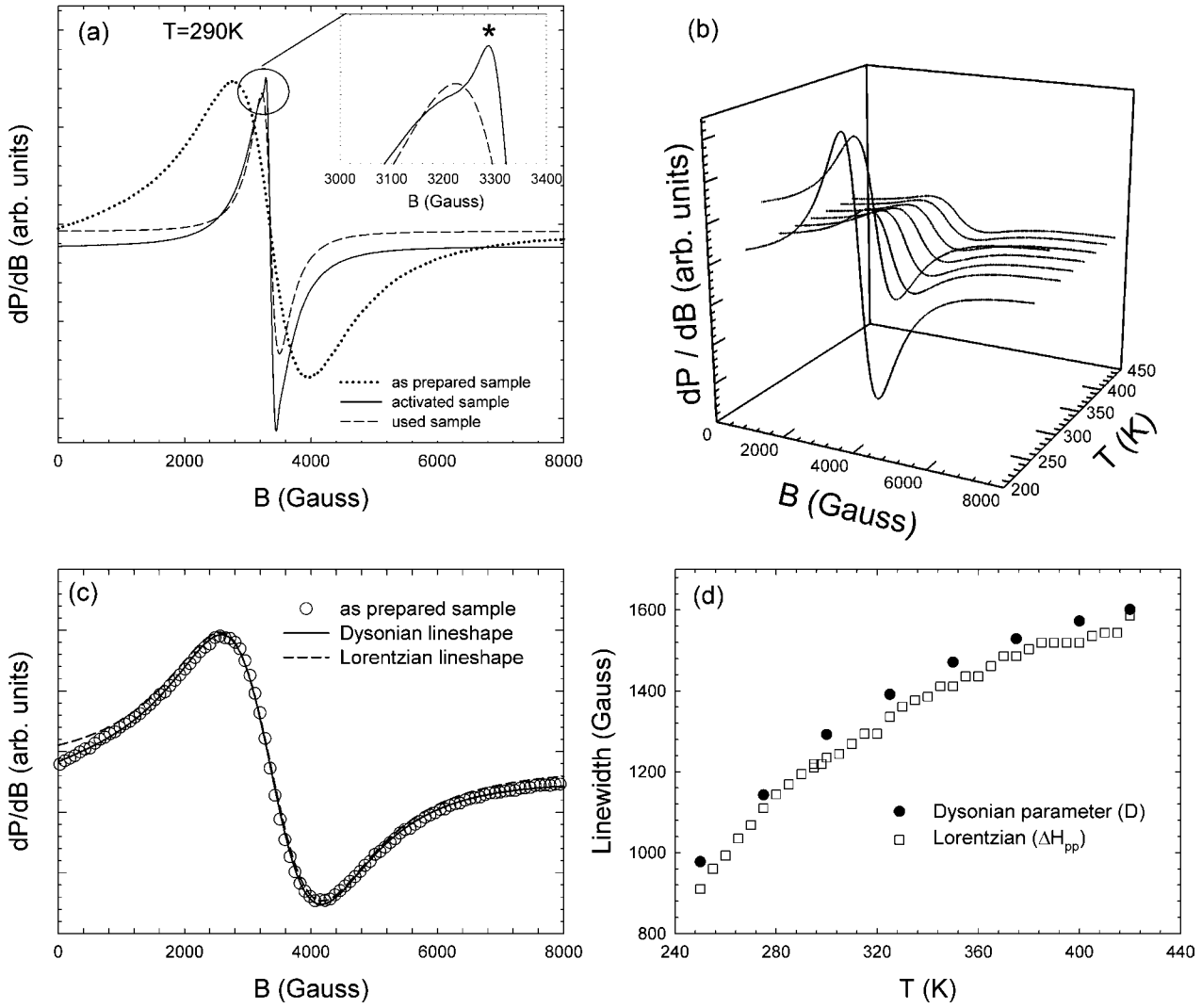

Figure 1. EPR spectra of $LaMnO_{3+\delta}$. (a) EPR spectra of as prepared sample (dotted line), after activation (solid line), after reaction (dashed line) at T = 290 K. (b) EPR spectra of the as prepared sample as a function of temperature; (c) EPR spectra of as prepared sample collected at T = 290 K (empty dots) fitted using a Dysonian (solid line) and Lorentzian (dotted line) functions; (d) Comparison between the parameters obtained by the Lorentzian model (ΔH_{pp}) and the Dysonian parameter (D) (see text for details).

min^{-1}. The pressure drop across the flame nozzle was set to 1.5 bar. The nanopowder so produced was collected by means of a 10 kV electrostatic precipitator.

Samples Structural Characterizations. XRPD patterns were collected using a Philips PW3020 powder diffractometer by employing the Ni-filtered Cu−K_α radiation. Patterns were collected in the range $20° \leq 2\theta \leq 80°$ with $\Delta 2\theta = 0.02°$ steps (5 s/step). The diffraction data were collected on as prepared samples and also after a thermal treatment similar to the activation preceding the catalytic tests. In addition, high resolution X-ray powder diffraction (HRXPD) measurements were performed at ID31 beamline of the ESRF. Data were collected in the $0 \leq 2\theta \leq 60°$ range at room temperature only on $LaMnO_{3+\delta}$ and $La_{0.9}Ce_{0.1}MnO_{3+\delta}$ as prepared samples by selecting a wavelength of λ = 0.35413(1) Å. Rietveld refinements were performed using the GSAS software suite of programs[11] and its graphical interface EXPGUI.[12] Background was subtracted using the shifted Chebyshev polynomials, and the diffraction peak profiles have been fitted with a modified pseudo-Voigt profile function. It should be noted that the accurate description of the line profile carried out in this work with the FP-prepared samples was made difficult because of the presence of a bimodal particle size distribution. To avoid overparametrization, just the line profile parameter (Lorentzian particle size broadening) was varied in the last refinement, together with background parameters, cell constants, and mean thermal parameter. Site occupancies have been fixed to the *nominal* values, and the atomic fractional coordinates have been taken from the neutron powder diffraction investigation.[13] The SSA of the synthesized powders was measured by N_2 adsorption/desorption at 77 K on a Micromeritics ASAP 2010 apparatus, after outgassing at 300 °C overnight. SEM analysis was carried out on a LEICA LEO 1420 instrument.

Catalysts Testing. Activity tests for the CFC of methane were performed by means of a continuous, 0.7 cm I.D., quartz tubular reactor on 0.15 g of catalyst, pelletized, ground and sieved to 0.15−0.25 mm particles. Prior to each run, activation was accomplished by treatment in flowing air (20 cm^3 min^{-1}), while increasing temperature by 10 °C min^{-1} up to 600 °C, then kept for 1 h. These pretreatment conditions were selected on the basis of a preliminary TPR-TPD-TPO investigation on various materials.[5,10] These activation conditions were adapted to fully saturate surface oxygen vacancies for most catalyst formulations, of course including those here analyzed, and to condition these samples at the highest temperature of catalysts testing, to avoid any sintering or phase modifications during the test. The activity tests were carried out by feeding 0.34 vol% CH_4, 33.3 vol% air, He balance, while increasing temperature by 10 °C min^{-1} from 200 °C up to 600 °C. Gas flow rate was regulated by means of mass flow controllers (Brooks Instruments, mod. 5850) governed by a control unit (Brooks, mod. 0154). The total gas flow rate was 30 mL min^{-1}. The outcoming gas was monitored in line by means of a quadrupolar mass

dx.doi.org/10.1021/ic300977e | Inorg. Chem. 2012, 51, 8433−8440

Table 1. Room-Temperature Structural Parameters for the As Prepared FP Samples

samples	$LaMnO_{3+\delta}$	$La_{0.9}Sr_{0.1}MnO_{3+\delta}$	$La_{0.81}Sr_{0.19}MnO_{3+\delta}$	$La_{0.9}Ce_{0.1}MnO_{3+\delta}$
space group	$P2_1/c$	$Pbnm$	$R\bar{3}c$	$P2_1/c$
a (Å)	7.925(2)	5.530(2)	5.5242(7)	7.929(3)
b (Å)	7.759(1)	5.526(2)		7.752(1)
c (Å)	7.894(1)	7.792(1)	13.3917(26)	7.850(1)
β (deg)	91.46(1)			91.49(2)
V (Å^3)	485.29(16)	238.12(4)	353.93(11)	482.35(20)
R_p (%)[a]	9.85	9.45	11.47	9.42

[a] R_p(%) = agreement factors between observed and calculated data.

spectrometer (MKS, PPT Residual Gas Analyzer), selecting proper mass fragments.

Catalyst poisoning was done in the same apparatus at 450 °C by injecting 0.6 mg of tetrahydrothiophene (THT, Fluka, pur. >97%) per g of catalyst after its first use. A standard activity test was repeated after every poisoning cycle.

EPR Analysis. X-band EPR measurements have been performed by a Bruker Elexsys EPR spectrometer equipped with an ER4102ST standard rectangular cavity and with a cryostatic ancillary apparatus. The EPR lines were fitted by the Bruker-XPR least-squares-based program. Data were collected with $La_{1-x}M_xMnO_{3+\delta}$ ($x = 0$ and $x = 0.1$ with M = Ce; Sr) as prepared and after two CFC reaction cycles alternated by sulfur poisoning by THT ("used" samples). $La_{0.81}Sr_{0.19}MnO_{3+\delta}$ was analyzed by EPR only on the as prepared sample.

RESULTS

General Considerations on the EPR Line-Shape of $LaMnO_{3+\delta}$. It is well know that the Sr^{2+} doping of $LaMnO_{3+\delta}$ favors the oxidation of Mn^{3+} to Mn^{4+}, giving rise to a mixed valence compound which displays a variety of phenomena such as electron conduction and ferromagnetic transition triggered, for example, by temperature.[8,14−16] In particular, concerning the origin of the EPR signal of $La_{0.9}Sr_{0.1}MnO_{3+\delta}$, it is widely reported that the spin relaxation behavior is linked with the double exchange interaction between Mn^{3+} and Mn^{4+} species.[8] In addition, the ferromagnetic resonance can also contribute to the spectrum at low T, because of ferromagnetic polarization arising around the Mn^{4+} ions.[8,14]

Conversely, the origin of the single EPR line observed with the undoped as prepared sample (Figure 1a) is rather intriguing. In principle, considering only the presence of Mn^{3+} species, the strong coupling between lattice, electronic, and magnetic degrees of freedom due to the static Jahn−Teller (JT) effect can be invoked to account for the origin of the EPR signal. In particular, the JT effect leads to a distortion of the oxygen octahedra of the undistorted cubic cell giving rise to an orthorhombic or monoclinic[13] structure. As a consequence, the e_g degeneracy is removed by lowering the energy of the occupied $d_{3x^2-r^2}$ or d_{3y2-r2} orbital. The Mn^{3+} ions acquire a zigzag-type ordering of occupied e_g orbitals in ab planes. By taking into account the spin−orbit coupling, an EPR signal is expected at about $g_z \cong 1.95$ and $g_x = g_y = 1.99$ which agrees very well with the experimental literature data.[14,17] Since $LaMnO_{3+\delta}$ remains JT distorted up to $T_{JT} = 750$ K,[18] the JT Mn^{3+} ground state could be considered almost temperature independent and no variation of the EPR peak-to-peak parameter is then expected at least below T_{JT}. However, we observe EPR line broadening with increasing temperature in the $250 \leq T \leq 420$ K range, as shown in Figure 1b for the as prepared $LaMnO_{3+\delta}$ sample. This cannot be explained by just invoking the static JT effect. Some spin−spin relaxation process must be hypothesized. Figure 1a shows the EPR spectra of different $LaMnO_{3+\delta}$ samples collected at $T = 290$ K. We note that the spectrum of the as prepared one (dotted line in Figure 1a) displays an exchange-narrowed EPR feature with a bit asymmetric shape, well described by the Dysonian model. The last suggests the presence of a rather high electron conductivity.[19,20] More precisely, the origin of this line shape can be attributed to an α dispersion-to-absorption contribution to the Lorentzian-shaped line. This effect occurs in samples in which the electron mobility is high enough to create a so-called "skin effect" for the microwave field employed by the EPR spectrometer. An $\alpha = 1$ value would correspond to dispersion of the same strength of absorption in a sample larger than its skin depth. On the opposite, in any case $\alpha = 0$ value with samples smaller than their skin depth. The present situation is the intermediate one, with $0 < \alpha < 1$.

Figure 1c shows the EPR spectra of the as prepared sample collected at $T = 290$ K, fitted using Dysonian and Lorenztian line shaped models. Although the low field part of the EPR spectra seems to be better described by the Dysonian one, a satisfactory agreement between observed and calculated data is obtained with both models. In the case of Lorentzian shaped line, the EPR peak-to-peak line-width ΔH_{pp} is equal to $(2/\sqrt{3})/T_2$ where T_2 is the spin−spin relaxation time. T_2 is provided also by the Dysonian fit of the line. To compare quantitatively the results provided by these two fitting procedures, the ΔH_{pp} values obtained by the Lorentzian fit are compared in Figure.1d to the D parameters calculated as $D = (2/\sqrt{3})W$, where $W = 1/T_2$ was derived from the Dysonian fit. We can observe that ΔH_{pp} can be reasonably retained as a good evaluation of D. Therefore, the Lorentzian model generally adopted to fit all the EPR spectra in the present study provides information not in contrast with the Dysonian one, concerning the trend of the relaxation time T_2 with temperature.

Samples Characterization. The fitting parameters obtained from the Rietveld refinement relative to $LaMnO_{3+\delta}$, $La_{0.9}Sr_{0.1}MnO_{3+\delta}$, $La_{0.81}Sr_{0.19}MnO_{3+\delta}$, and $La_{0.9}Ce_{0.1}MnO_{3+\delta}$ are reported in Table 1. $LaMnO_{3+\delta}$ and $La_{0.9}Ce_{0.1}MnO_{3+\delta}$ samples were monoclinic at room temperature, space group $P2_1/c$[13] unlike $La_{0.9}Sr_{0.1}MnO_{3+\delta}$ and $La_{0.81}Sr_{0.19}MnO_{3+\delta}$ samples, which resulted to be orthorhombic, space group $Pbnm$[13] and rhombohedric, space group $R\bar{3}c$, respectively.

Relatively high values of the accordance parameter (R_p in Table 1) are obtained. This is caused by the broadening of reflections as a result of the bimodal particle distribution in all the FP samples. In the present cases, the diffraction peaks can be described by more than one pseudo-Voigt function, characterized by different profile parameters. Hence, with such profiles the determination of the size of the crystallites

dx.doi.org/10.1021/ic300977e | Inorg. Chem. 2012, 51, 8433−8440

from the XRPD patterns is far from trivial. Accurate line profile analyses will be the subject of further studies.

The HRXPD patterns of the as prepared $LaMnO_{3+\delta}$ and $La_{0.9}Ce_{0.1}MnO_{3+\delta}$ samples are compared in Figure 2. The region put in evidence in the inset is where the (111) peak of CeO_2 (e.g., $Fm\bar{3}m$) would be expected. No contribution of a well crystallized CeO_2 phase can be found in our HRXPD data, in spite of the fact that the presence of a segregated CeO_2 second phase is generally reported in the literature[21] for a $La_{0.9}Ce_{0.1}MnO_{3+\delta}$ prepared by solid state reaction. This suggests that the substitution of La for Ce actually occurs in our FP-prepared material.[22]

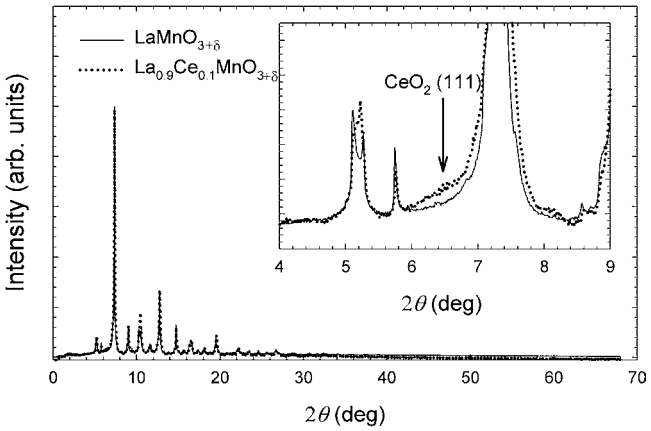

Figure 2. Synchrotron radiation powder diffraction patterns for $LaMnO_{3+\delta}$ (solid line) and $La_{0.9}Ce_{0.1}MnO_{3+\delta}$ (dotted line) collected at room temperature. The inset shows the pattern region where the (111) peak of CeO_2 is expected at λ = 0.35413 Å.

A rhombohedral (e.g., $R\bar{3}c$)[13] structural model gave the best agreement with the data observed with activated $LaMnO_{3+\delta}$ and $La_{1-x}Sr_xMnO_{3+\delta}$ samples (not shown), whereas the orthorhombic (e.g., *Pbnm*)[13] model was suitable to interpret the $La_{0.9}Ce_{0.1}MnO_{3+\delta}$ sample (not shown). The observed phase transitions are fully compatible with an increase of the Mn^{4+} concentration inside the material, according to the structural phase diagram proposed by Mitchell et al.[13] Hence, the activation process preceding the catalytic test favors the oxidation of Mn^{3+} to Mn^{4+} in all the FP-samples.

SSA was 56, 84, and 51 m^2/g for $LaMnO_{3+\delta}$, $La_{0.9}Ce_{0.1}MnO_{3+\delta}$, and $La_{0.9}Sr_{0.1}MnO_{3+\delta}$, respectively. After activation at 600 °C and testing, SSA is expected to decrease. In a previous extensive investigation on the effect of thermal treatment on parent FP-prepared samples,[22] we observed that, rather independently of the initial SSA of the catalyst, the residual SSA was still about 20 $m^2\ g^{-1}$ after calcination at 600 °C for 1 h.

The FP-prepared x = 0 sample, as well as the (x = 0.1) M = Ce one, showed a single $g \cong 2$ nearly symmetric EPR line at least in the temperature range 250 < T < 420 K. A computer-aided spectral shape fitting was obtained for this pattern (*vide infra*). That feature was broader than that of the literature materials with identical chemical composition, but prepared by SG synthesis.[8,23] Furthermore, with the FP freshly prepared catalysts (Figure 3a) the line-width was continuously increasing with increasing temperature, at difference with the analogous

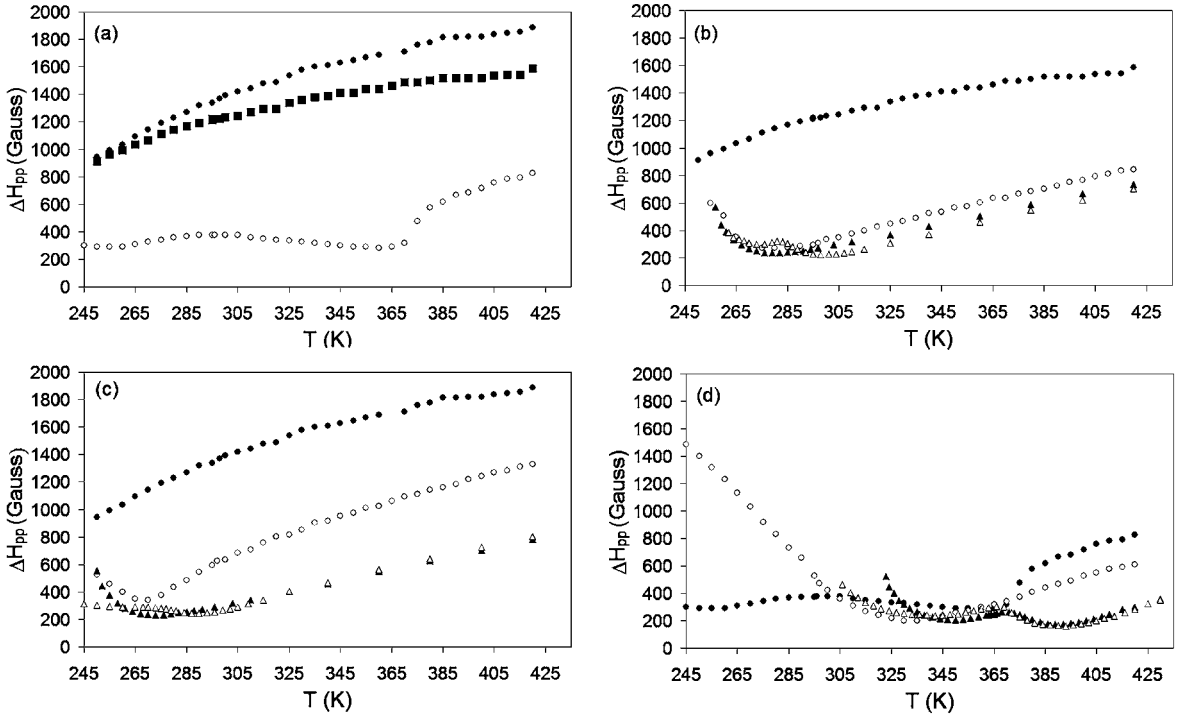

Figure 3. Temperature dependences of peak-to-peak width (ΔH_{pp}) of the $g \cong 2$ EPR line observed. The ΔH_{pp} values refer to (a) $La_{0.9}Ce_{0.1}MnO_{3+\delta}$ (full circles), $LaMnO_{3+\delta}$ (full squares), $La_{0.9}Sr_{0.1}MnO_{3+\delta}$ (empty circles) FP as prepared samples; (b) $LaMnO_{3+\delta}$-FP as prepared (full circles) and used (empty circles) samples and $LaMnO_{3+\delta}$-SG as prepared (full triangles) and used (empty triangles) samples; (c) $La_{0.9}Ce_{0.1}MnO_{3+\delta}$-FP as prepared (full circles) and used (empty circles) samples and $La_{0.9}Ce_{0.1}MnO_{3+\delta}$-SG as prepared (full triangles) and used (empty triangles) samples; (d) $La_{0.9}Sr_{0.1}MnO_{3+\delta}$-FP as prepared (full circles) and used (empty circles) samples and $La_{0.9}Sr_{0.1}MnO_{3+\delta}$-SG as prepared (full triangles) and used (empty triangles) samples.

dx.doi.org/10.1021/ic300977e | *Inorg. Chem.* 2012, 51, 8433−8440

SG-prepared materials (full triangles in Figure.3b–d) for which the line-width vs temperature revealed a relative minimum at $T = T_{min}$, as typical in the presence of a magnetic transition.[8] However, the last kind of trend, accompanied by line-narrowing, was observed also with the FP-prepared undoped and Ce-doped catalysts after chemical reaction (empty circles in Figure 3b and c).

A more complicated behavior was observed with the M = Sr, $x = 0.1$ sample. Indeed, the partial substitution of Sr for La caused a very dramatic EPR line narrowing, as shown in Figure 3a. Furthermore, with M = Sr no Lorentzian or Gaussian or Dysonian shape was able to fit the experimental patterns. A deeper examination suggested that they were formed of many overlapping contributions, all with nearly the same g value but different width. To analyze more carefully such a behavior, a wider $115 < T < 450$ K temperature range was explored with the $x = 0.1$, M = Sr sample, and the data are shown in Figure 4.

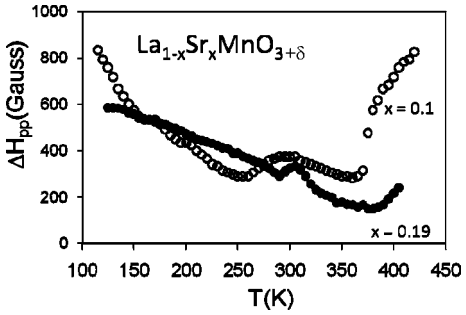

Figure 4. Temperature dependence of ΔH_{pp} of the $g \cong 2$ EPR related to $La_{0.9}Sr_{0.1}MnO_{3+\delta}$ (full circles) and $La_{0.81}Sr_{0.19}MnO_{3+\delta}$ (empty circles) as prepared FP samples.

At least two different line-width minima were observed at different temperatures. All these peculiarities of the M = Sr, $x = 0.1$ sample compelled us to analyze also the EPR spectrum of the Sr-doped sample with $x = 0.19$ (Figure 4 (full circles)). The overlapping of a few EPR features resulted even more evident in this case, still accompanied by more than one minimum in the trend of the ΔH_{pp} of the overall pattern vs T. Furthermore, ΔH_{pp} was smaller with $x = 0.19$ even than with $x = 0.1$, for $310 < T < 410$ K (at least). For example, $\Delta H_{pp} = 700$ G and $\Delta H_{pp} = 250$ G were evaluated at 400 K with $La_{1-x}Sr_xMnO_{3+\delta}$ in the cases of $x = 0.1$ and of $x = 0.19$, respectively.

The EPR line-narrowing occurring after catalytic reaction was more marked with the undoped (Figure 3b) than with the Ce-doped (Figure 3c) and with the Sr-doped (Figure 3d) FP samples. However, we must outline that before reaction the Sr-doped sample was already characterized by the narrowest EPR feature, as above-mentioned. After catalytic reaction, $T_{min} \cong 270$, 280, and 340 K with the Ce-doped, undoped and Sr-doped ($x = 0.1$) samples, respectively.

Some as prepared samples have been examined by EPR also after a thermal activation process in air analogous to that which was employed before their catalytic use (see for example inset of Figure 1a). A marked EPR line narrowing was always observed after this treatment, as was noticed with the same samples after catalytic reaction (*vide infra*). Furthermore, after activation of the undoped sample a second even narrower EPR appeared at $T < \sim 330$ K. This feature is marked with a star in the EPR collected at 290 K shown in the inset of Figure 1a.

Both the M = Sr samples showed satisfactorily resistance to sulfur poisoning.[5] The CH_4 conversion obtained with all these samples vs reaction temperature is reported in Figure 5. The $x = 0.1$, M = Sr catalyst was the best performing at $T > 370$ °C.

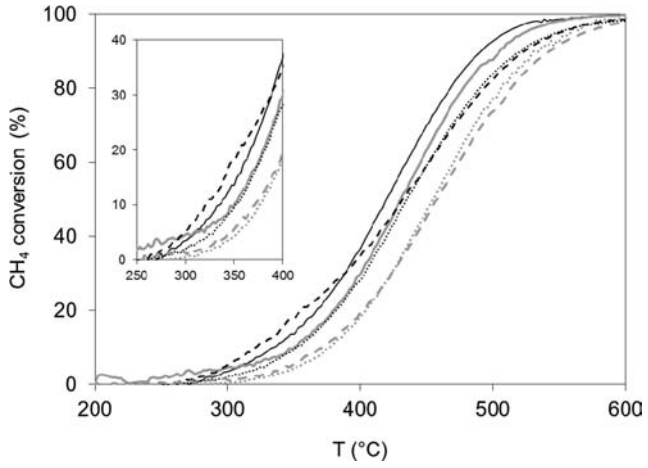

Figure 5. CH_4 conversion vs reaction temperature. $LaMnO_{3+\delta}$ (dotted line), $La_{0.9}Ce_{0.1}MnO_{3+\delta}$ (dashed line), $La_{0.9}Sr_{0.1}MnO_{3+\delta}$ (continuous line). As-prepared catalysts: black lines, poisoned samples: gray lines. Inset: detail of the low temperature performance of the catalysts.

However, attempts to further improve activity with increasing Sr doping failed, since the $x = 0.19$, M = Sr sample was not more active than the undoped one.[5] The M = Ce sample proved the best performing at lower temperature among the fresh samples, but its low-temperature activity was completely lost after poisoning (Figure 5). Some of these features were compared to those reported elsewhere[8] for samples with the same chemical composition, but prepared by the SG procedure and characterized by a surface area 5 to 10 times smaller than for the present samples. In any case, the FP-prepared catalysts were by far more active than the analogous SG-prepared ones.

DISCUSSION

General Considerations. Temperature-broadened single EPR lines for $LaMnO_{3+\delta}$ based systems have been already reported with the above-mentioned SG-prepared samples of chemical compositions identical to those here examined. Those features were attributed to the temperature-dependent interactions between phonons and conduction electrons (i.e., to polarons formation).[8,23] However, those catalysts showed an EPR line narrower (empty and full triangles in Figure 3b-d) than in the present case (empty and full circles in the same panels of Figure 3) at the same T and chemical composition. Indeed, the EPR line of the here examined FP-prepared samples was about 2–3 times (1.3 times with M = Sr) broader than those of the analogous SG-prepared materials, at least in the range of ~ 280 (380 with M = Sr) $< T < 420$ K.

EPR lines broader than with SG samples were already reported and discussed for Flame-Hydrolysis (FH) prepared undoped La Manganite at room temperature.[23] An apparently similar EPR pattern was there reported also with an amorphous SG-prepared sample but that feature was temperature independent and the sample was by far less durable than all the crystalline ones examined there and in the present investigation. The observed differences in EPR line-width can be related to different structural sample phases. Indeed, undoped Manganite was rhombohedral when SG-prepared, orthorhombic when FH-prepared,[23] and monoclinic in the present FP-prepared sample.

dx.doi.org/10.1021/ic300977e | Inorg. Chem. 2012, 51, 8433–8440

According to Mitchell et al.,[13] the crystal structure of undoped and Sr-doped $LaMnO_{3+\delta}$ materials (at fixed T) is strictly connected to the Mn^{4+} concentration (hereinafter $[Mn^{4+}]$) inside the structure. In particular, for a full cation stoichiometry (formal Mn valence state +3) the monoclinic distortion is observed. Phase transitions to the orthorhombic and then to the rhombohedral phase occur at greater $[Mn^{4+}]$ values.

It has been reported[8] that SG undoped and Ce-doped orthorhombic samples were able to undergo a transition from paramagnetic (PM) to ferromagnetic (FM) state. This was argued from their EPR spectra at enough low temperature, which assumed the broadened asymmetric shape typical of FM resonance features. The last were characterized by the peak-to-peak width here reported by full triangles in Figure 3b,c to compare them to the EPR line-widths (full circles in the same figure) observed in the present work with the FP-prepared monoclinic samples. The latter were characterized by the same chemical composition of the former, but no line-shape changing and broadening due to PM to FM transition was observed with them. This can be attributed to a lower abundance of Mn^{4+} ions present in the monoclinic with respect to the orthorhombic crystal lattice, leading to a lower amount of free electrons available to form FM domains.

After activation, FP $LaMnO_{3+\delta}$ and $La_{0.9}Sr_{0.1}MnO_{3+\delta}$ samples belong to a rhombohedral structural phase while $La_{0.9}Ce_{0.1}MnO_{3+\delta}$ sample is orthorhombic. The latter structure suggests that the Ce^{4+} ions are hosted in the $La_{0.9}Ce_{0.1}MnO_{3+\delta}$ perovskite-like lattice, the decreasing of the Mn^{4+}/Mn^{3+} ratio inhibiting the rhombohedral distortion and even favoring the reduction of some Mn^{3+} to Mn^{2+}. Therefore, after activation the Ce-doped catalyst behaves rather analogously to the undoped one (empty circles in Figure 3b,c). Indeed, both remain homogeneous materials, as revealed by their EPR spectrum which retains its nearly Dysonian shape at $T > 300$ K.

Both the FM transition at low temperature and the EPR line narrowing (with respect to fresh samples), when occurring with the used samples or after activation in air, could be attributed to an increased particle size due to partial sintering. However, in the present case this would contrast with the thermal stability of these FP-prepared catalysts.[10,22] Therefore, only the phase transition from monoclinic to orthorhombic/rhombohedral can be invoked to account for the FM transition and for the EPR line narrowing, also in the case of used and of activated samples.

All these considerations essentially allow a better understanding of the catalytic properties of these materials. It has been already reported[5] that the catalytic activity for the CFC of methane follows different mechanisms with increasing temperature. Indeed, at low temperature the oxidation of the substrate would be mediated by surface oxygen (*suprafacial* mechanism), accounting for a limited methane conversion. Satisfactory catalytic activity may be attained with these catalysts at high temperature only, because of a key role played by the oxygen mobility through the perovskite-like lattice (*intrafacial* mechanism). In this regard, it is worth to note that the best catalyst at $T < 370$ °C was no more the Sr-doped but the Ce-doped one (Figure 5), though for the first reaction cycle only. This confirms that, during the first reaction cycle, the CFC of methane partly follows a suprafacial mechanism.[5] This supports the presence of surface oxygen induced by the substitution of Ce^{4+} for La^{3+}, in agreement with the diffraction data. The decreased performance of the Ce-doped catalyst after poisoning is easily explained on the basis of the same poisoning mechanism. Indeed, surface poisoning with sulfur employs surface oxygen to form sulphites or sulphates, with consequent depression of the low temperature suprafacial activity which is based on the availability of surface oxygen.

Interplay between EPR Line Broadening Mechanism and the CFC Performance. It has been above stated that in the CFC the oxygen mobility plays a key role at higher temperature only. This process can be easily figured out by a Mars Van Krevelen (MvK) mechanism.[24] In the methane CFC performed on Mn-based perovskite, the MvK model can be composed of two steps: (*a*) the reduction of the Mn^{4+} to Mn^{3+} species, accompanied by lattice oxygen depletion; (*b*) the subsequent oxidation of the Mn^{3+} species by the oxygen cofed with CH_4 during the CFC reaction.

If steps (*a*) and (*b*) occur simultaneously, one can identify the CFC as a redox or a regenerative mechanism.[25] It should be noted that in our case, before the CFC experiment, the sample undergoes an activation process. The Rietveld refinement of the activated samples shows that the structure of all the samples is rhombohedral (e.g., $R\bar{3}c$) indicating that the activation process increases the Mn^{4+} concentration in the materials. This process is accompanied by the formation of cationic vacancies of type: V_{Mn}''', V_{La}''' expressed in the Kröger-Vink notation, as reported elsewhere.[13]

Since the MvK mechanism is controlled by the oxidation and reduction of Mn, we can argue that, given the high spin electronic configurations of Mn^{3+} $t_{2g}^3e_g^1$ and Mn^{4+} $t_{2g}^3e_g^0$, the electronic delocalization of the Mn^{3+} e_g spin between Mn^{3+} and Mn^{4+} could assist the MvK mechanism during the CFC reaction. On the other hand, the double-exchange (DE) between Mn^{3+} and Mn^{4+} can account for this electronic delocalization. The last is also in agreement with the Dysonian EPR line shape, typical of electron mobility in conducting systems. This leads to a direct connection between the DE and the MvK mechanism.

However, all these Dysonian shaped EPR features affected by DE were found in the undoped as prepared sample which can be considered Mn^{4+} free. Furthermore, the EPR line after the activation process changed markedly (inset in Figure.1a). This suggests that a more complex mechanism may exist. Much experimental evidence[26−30] indicate that the thermally activated disproportion $2Mn^{3+} \rightarrow Mn^{2+} + Mn^{4+}$ can easily occur in $LaMnO_{3+\delta}$. This process is facilitated both by the ease of the $Mn^{3+} \rightarrow Mn^{4+} + 1\ e^-$ oxidation process and by the fact that the latter ions stabilize the perovskite-like lattice because of their smaller size. Therefore, $[Mn^{4+}]$ is increased by annealing the sample in air. This leads to the overlapping EPR lines shown in the inset of Figure.1a, where the narrower line is attributable to Mn^{2+} ions[14] and the broader one is due to Mn^{3+}-O-Mn^{4+}.[8,31] The same process affects the samples after catalytic reaction (see Figure 3b).

By taking the disproportion process $2Mn^{3+} \rightarrow Mn^{2+} + Mn^{4+}$ as a reference, we can now discuss the interplay between the catalytic activity and the DE linked to MvK mechanism for the doped samples. The substitution of a Ce^{4+} for a La^{3+} ion is equivalent to the introduction of one electron, which reduces one Mn^{3+} to Mn^{2+}, increasing its concentration in the disproportion process. The ΔH_{pp} of the Ce-doped as prepared sample is compared in Figure 3a with that of the undoped one. The broader line of the former could be attributed to a (temperature dependent) decreased efficiency of DE line-narrowing mechanism. To explain this, we consider that the

dx.doi.org/10.1021/ic300977e | Inorg. Chem. 2012, 51, 8433−8440

Mn^{2+}-Mn^{4+} ions can form Electron−Hole (EH) pairs.[32−34] It has been also reported that the EH pairs have a very large fluctuating electrical dipole moment causing an attractive electrostatic dipole−dipole interaction which group themselves into an EHBL (Bose Liquid) phase. Hence this may subtract some Mn^{4+} ions from the DE. Indeed, Mn^{3+} is by far the more abundant Mn species present in the sample, so that a decreased amount of Mn^{4+} only is sufficient to cause a decreased DE and, hence, a depletion in the CFC activity. This is in agreement with the decreased activity of Ce-doped with respect to undoped $LaMnO_{3+\delta}$ (Figure 5), observed at high temperature, that is, when the catalytic activity is fully explained by the MvK mechanism.

By contrast, doping $LaMnO_{3+\delta}$ by Sr^{2+} increases the $[Mn^{4+}]$ in the material. This is confirmed both by the XPRD data and by the EPR line shape, which is by far narrower with the $x = 0.1$ Sr-doped catalyst than with the undoped and Ce-doped samples (Figure 3a), becoming even narrower when $x \cong 0.2$ (Figure 4). This strong narrowing can be attributed to an increased Mn^{4+}−O−Mn^{3+} DE, favored by the greater availability of Mn^{4+} ions,[8,15] as well as by the smaller distortion of the Mn−O−Mn bond angle arising from the substitution of Sr^{2+} for La^{3+}.[35] Hence, according to the MvK model, since the DE spin enhances the electronic delocalization from Mn^{3+} to Mn^{4+} e_g level, the activity for the CFC reaction must increase with increasing Sr content. This is in agreement with Figure 5, showing the catalytic conversion with undoped and $x = 0.1$ doped catalysts. However, unexpectedly, no further increase of the catalytic activity was noticed with the $La_{0.81}Sr_{0.19}MnO_{3+\delta}$ sample, but, instead, the conversion was comparable to that of the undoped catalyst,[5] suggesting that an even more complicated mechanism must be hypothesized.

One of the possible explanations could be that during the activation process the material could reach the oxygen saturation condition described by Mizusaki et al.[36] In particular, the oxidation of Mn^{3+} in $LaMnO_{3+\delta}$ upon Sr doping leads to the formation of Sr_{La}' defects whereas the activation process induces the formation of cationic vacancies (V_{Mn}''', V_{La}'''). As proposed by Mizusaki et al., the interactions between the V_{Mn}''', V_{La}''', Sr_{La}' defects give rise to the expansion of the crystal lattice around the Sr_{La}' to minimize the electrostatic repulsion. However, this expansion could be corrupted at high Sr amounts because of a decreased amount of the cationic vacancies. In addition, when high amount of Sr_{La}' is induced because of doping, the compensation of the negative charge yields the formation of double-ionized oxygen vacancy instead of Mn^{4+} single hole species.[37] All these aspects can support a depletion of Mn^{4+} and the depletion of the activity observed for the $x = 0.19$ sample.

CONCLUSIONS

Flame pyrolysis preparation of undoped and Ce-doped samples leads to nanoparticles with monoclinic structure, whereas Sr-doped catalysts show orthorhombic/rhombohedral symmetry. The observed structural phases can be linked to the amount of Mn^{4+} present in the Sr doped samples, and to the fact that the undoped and the Ce-doped samples are almost Mn^{4+} free.

The EPR measurements indicate that all paramagnetic Mn^{2+}, Mn^{3+}, and Mn^{4+} ions contribute to the EPR spectrum, though by different mechanisms, among which (*i*) Mn^{3+}−O−Mn^{4+} DE, favoring electron mobility, and (*ii*) disproportion of Mn^{3+} into Mn^{4+} and Mn^{2+} ions. In particular, the latter mechanism can account for the DE between Mn^{3+} and Mn^{4+} occurring in the presence of Mn^{2+} ions, observed with the undoped sample after activation.

The $x = 0.1$ Sr-doped catalyst was the most active for the CFC reaction at high temperature. This is attributed to the higher concentration of Mn^{4+} ions, favoring the electron delocalization through the -Mn^{3+}-O-Mn^{4+}- chains (as revealed by the DE causing EPR line narrowing). The last process would assist the MvK mechanism, which dominates in the CFC reaction at high temperature. At $x > 0.1$ a Sr-doped sample showed a decreased catalytic performance, even if the DE increased with respect to the undoped and with the $x = 0.1$ Sr-doped samples. This can be attributed to oxygen saturation conditions and/or to formation of double-ionized oxygen vacancies instead of Mn^{4+} single holes species.

Conversely, the best catalyst at $T < 370$ °C is the Ce-doped sample, though for the first CFC cycle only. This indicates that the CFC of methane, for this catalyst, partly follows a suprafacial mechanism before surface poisoning, supporting the involvement of surface oxygen.

AUTHOR INFORMATION

Corresponding Author

*E-mail: cesare.oliva@unimi.it. Phone: +39 0250314270. Fax: +39 0250314300.

Notes

The authors declare no competing financial interest.

ACKNOWLEDGMENTS

The authors are indebted with Serena Cappelli for EPR spectra collection and simulation, as well as for helpful discussion.

REFERENCES

(1) Tanaka, H.; Mizuno, N.; Misono, M. *Appl. Catal., A* **2003**, *244*, 371−382.
(2) Choi, Y. M.; Lynch, M. E.; Lin, M. C.; Liu, M. *J. Phys. Chem. C* **2009**, *113*, 7290−7297.
(3) Kaddouri, A.; Gelin, P.; Dupont, N. *Catal. Commun.* **2009**, *10*, 1085−1089.
(4) Li, Y.; Xue, L.; Fan, L.; Yan, Y. *J. Alloys Compd.* **2009**, *478*, 493−497.
(5) Rossetti, I.; Buchneva, O.; Biffi, C.; Rizza, R. *Appl. Catal., B* **2009**, *89*, 383−390.
(6) Peña, M. A.; Fierro, J. L. G. *Chem. Rev.* **2001**, *101*, 1981−2018.
(7) Tsai, Y. T.; Chang, W. J.; Wuang, S. W.; Lin, J.-Y.; Lee, J. Y.; Chen, J. M.; Wu, K. H.; Uen, T. M.; Gou, Y. S.; Juang, J. Y. *Phys. B* **2009**, *404*, 1404−1408.
(8) Oliva, C.; Forni, L.; Pasqualin, P.; D'Ambrosio, A.; Vishniakov, A. V. *Phys. Chem. Chem. Phys.* **1999**, *1*, 355−360.
(9) Strobel, R.; Pratsinis, S. E. *J. Mater. Chem.* **2007**, *17*, 4743−4756.
(10) Chiarello, G. L.; Rossetti, I.; Forni, L.; Lopinto, P.; Migliavacca, G. *Appl. Catal., B* **2007**, *72*, 218−226 and 227−232.
(11) Larson, A. C.; Von Dreele, R. B. *General Structure Analysis System. (GSAS)*, Los Alamos National Laboratory Report LAUR 86-748; Los Alamos National Laboratory: Los Alamos, NM, 2004
(12) Toby, B. H. *J. Appl. Crystallogr.* **2001**, *34*, 210−213.
(13) Mitchell, J. F.; Argyriou, D. N.; Potter, C. D.; Hinks, D. G.; Jorgensen, J. D.; Bader, S. D. *Phys. Rev. B* **1996**, *54*, 6172−6183.
(14) Ivanshin, V. A.; Deisenhofer, J.; Krug von Nidda, H. A.; Loidl, A.; Mukhin, A. A.; Balbashov, A. M.; Eremin, M. V. *Phys. Rev. B* **2000**, *61*, 6213−6219.
(15) Noginova, N.; Bah, R.; Bitok, D.; Atsarkin, V. A.; Demidov, V. V.; Gudenko, S. V. *J. Phys.: Condens. Matter* **2005**, *17*, 1259−1269.
(16) Rozenberg, E.; Auslender, M.; Shames, A. I.; Mukovskii, Ya.M.; Sominski, E.; Gedanken, A. *J. Appl. Phys.* **2009**, *105* (07D707), 1−3.

(17) Abragham, A.; Bleaney, B. *EPR of Transition Ions*; Oxford University Press: Oxford, U.K., 1970.
(18) Rodrìguez-Carvajal, J.; Hennion, M.; Moussa, F.; Moudden, A. H.; Pinsard, L.; Revcolevschi, A. *Phys. Rev. B* **1998**, *57*, R3189−R3192.
(19) Feher, G.; Kip, A. F. *Phys. Rev.* **1955**, *98*, 337−348.
(20) Dyson, F. J. *Phys. Rev.* **1955**, *98*, 349−359.
(21) Mitra, C.; Raychaudhuri, P.; John, J.; Dhar, S. K.; Nigam, A. K.; Pinto, R. *J. Appl. Phys.* **2001**, *89*, 524−530.
(22) Chiarello, G. L.; Rossetti, I.; Forni, L. *J. Catal.* **2005**, *236*, 251−261.
(23) Oliva, C.; Forni, L. *Catal. Commun.* **2000**, *1*, 5−8.
(24) Vannice, M. A. *Catal. Today* **2007**, *123*, 18−22.
(25) Doornkamp, C.; Ponec, V. *J. Mol. Catal. A: Chem.* **2000**, *162*, 19−32.
(26) Zhou, J. S.; Goodenough, J. B. *Phys. Rev. B* **1999**, *60*, R15002−R15004; and *Phys. Rev. B* **2003**, *68*, 144406−144411.
(27) Raffaelle, R.; Anderson, H. U.; Sparlin, D. M.; Parris, P. E. *Phys. Rev. B* **1991**, *43*, 7991−7999.
(28) Hundley, M. F.; Neumeier, J. J. *Phys. Rev. B* **1997**, *55*, 11511−11515.
(29) Ahlgren, E. O.; Poulsen, F. W. *Solid State Ionics* **1996**, *86*−*88*, 1173−1178.
(30) Buch, J. J. U.; Pathak, T. K.; Lakhani, V. K.; Vasoya, N. H.; Modi, K. B. *J. Phys. D* **2007**, *40*, 5306−5312.
(31) Oseroff, S. B.; Torikachvili, M.; Singley, J.; Ali, S.; Cheong, S. W.; Schultz, S. *Phys. Rev. B* **1996**, *53*, 6521−6525.
(32) Moskvin, A. S. *Phys. B* **1998**, *252*, 186−197.
(33) Moskvin, A. S.; Avvakumov, I. D. *Phys. B* **2002**, *322*, 371−389.
(34) Moskvin, A. S. *Phys. Rev. B* **2009**, *79* (115102), 1−19.
(35) Asamitsu, A.; Moritomo, Y.; Tomioka, Y.; Arima, T.; Tokura, Y. *Nature* **1995**, *373*, 407−409.
(36) Mizusaki, J.; Mori, N.; Takai, H.; Yonemura, Y.; Minamiue, H.; Tagawa, H.; Dokiya, M.; Inaba, H.; Naraya, K.; Sasamoto, T.; Hashimoto, T. *Solid State Ionics* **2000**, *129*, 163−177.
(37) Yasuda, I.; Hishinuma, M. *J. Solid State Chem.* **1996**, *123*, 382−390.